Journal of Energy Storage 154 (2026) 121234

Contents lists available at ScienceDirect

Journal of Energy Storage

journal homepage: www.elsevier.com/locate/est

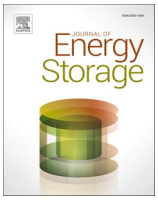

Research Papers

Electroactive redox-active pyrene and hexaazatriphenylene-based conjugated microporous polymers as positive electrode with MXene film as negative electrode for high-performance asymmetric supercapacitor electrode

Mohamed Gamal Mohamed [a,b,1,*], Poonam Nagendra Singh [a,1], Elangovan Sivasurya [c,d,1], Reeba Mary Mammen [a], Hira Karim [e], Ahmed F. Saber [f], Pramod K. Kalambate [g], Devaraj Manoj [c,d,**], Da-Ren Hang [a,***], Shiao-Wei Kuo [a,h,*]

[a] Department of Materials and Optoelectronic Science, Center for Functional Polymers and Supramolecular Materials, National Sun Yat-Sen University, Kaohsiung, 804, Taiwan
[b] Chemistry Department, Faculty of Science, Assiut University, Assiut, 71515, Egypt
[c] Department of Chemistry, Karpagam Academy of Higher Education, Coimbatore, 641021, India
[d] Centre for Material Chemistry, Karpagam Academy of Higher Education, Coimbatore, 641021, India
[e] Department of Chemistry, School of Natural Sciences (SNS), National University of Sciences and Technology (NUST), H-12, Islamabad, 44000, Pakistan
[f] Interdisciplinary Research Center for Hydrogen Technologies and Carbon Management (IRC-HTCM), King Fahd University of Petroleum & Minerals, Dhahran, 31261, Saudi Arabia
[g] Department of Chemistry & Waterloo Institute for Nanotechnology, University of Waterloo, Waterloo, Ontario, Canada
[h] Department of Medicinal and Applied Chemistry, Kaohsiung Medical University, Kaohsiung, 807, Taiwan

ARTICLE INFO

Keywords:
Pyrene
Hexaazatriphenylene
Conjugated microporous polymer
Redox unit
Pseudocapacitive
Asymmetric device
Supercapacitors

ABSTRACT

We herein present the development of conjugated microporous polymers (CMP), PTB–HATN CMP, meticulously engineered through a highly efficient Sonogashira coupling reaction between tetraethynylpyrene (PTB) and hexabromodiquinoxalino[2,3-a:2′,3′-c]phenazine (HATN-6Br). The resulting conjugated framework features an interconnected microporous–mesoporous architecture, endowing it with a substantial Brunauer–Emmett–Teller (BET) surface area of 198 $m^2\ g^{-1}$. The PTB–HATN CMP as positive electrode displayed pronounced pseudocapacitive behavior, arising from the synergistic interplay of its abundant redox-active sites, π-conjugated pyrene units, and electron-deficient HATN cores. Notably, PTB–HATN CMP electrode exhibited a specific capacitance (SC) of 1010.2 F g^{-1} at 1 A g^{-1}, surpassing the performance of many previously reported conjugated polymers and CMP-based electrodes in 3 M H_2SO_4. Moreover, excellent cyclic stability with almost 99% columbic efficiency was maintained for all cycles, and also retained 97.6% of its capacitance for continuous 5000 charge–discharge cycles, highlighting its robustness and practical potential for energy storage applications. Moreover, when all pseudocapacitive electrodes, namely MXene ($Ti_3C_2T_x$) film as negative electrode and PTB–HATN CMP as positive electrode, are integrated, the resultant asymmetric supercapacitor device (ASC) of $Ti_3C_2T_x$//PTB-HATN CMP, which enhances the charge storage capability via all pseudocapacitive redox active sites, achieves a high SC value of 230 F g^{-1} at 1 A g^{-1}. This work showcases the promising impact of rationally designed CMPs integrated with MXene film, positioning them as next-generation materials that offer a versatile and powerful pathway for advancing electrochemical energy storage technologies.

* Corresponding authors at: Department of Materials and Optoelectronic Science, Center for Functional Polymers and Supramolecular Materials, National Sun Yat-Sen University, Kaohsiung, 804, Taiwan.
** Correspondence to: D. Manoj, Department of Chemistry, Karpagam Academy of Higher Education, Coimbatore, 641021, India.
*** Corresponding author.
E-mail addresses: mgamal.eldin12@yahoo.com, mgamal.eldin12@mail.nsysu.edu.tw (M.G. Mohamed), manojdvrj@gmail.com, manoj.devaraj@kahedu.edu.in (D. Manoj), drhang@faculty.nsysu.edu.tw (D.-R. Hang), kuosw@faculty.nsysu.edu.tw (S.-W. Kuo).
[1] These authors contributed equally.

https://doi.org/10.1016/j.est.2026.121234
Received 2 October 2025; Received in revised form 6 February 2026; Accepted 19 February 2026
Available online 24 February 2026

1. Introduction

The growing depletion of fossil fuel reserves, coupled with their adverse environmental impacts, has intensified the demand for renewable energy sources and efficient energy storage technologies [1–5]. Consequently, the design of environmentally friendly and robust energy generation and storage platforms has become a major research focus. Despite major advances in energy conversion technologies, progress in batteries, organic solar cells (OSCs), and energy storage systems remains limited [1–3,6–12]. To address this gap, various energy storage systems have been investigated, among which supercapacitors (SCs) have attracted considerable attention. Due to their promising applications in modern energy storage [13–17]. SCs offer several advantageous properties, including long cycle life, high power density, stable performance, and rapid charge–discharge capability, rendering them highly adaptable for broad energy storage purposes [18–21]. Although their energy density is generally lower than that of conventional batteries, these characteristics establish SCs as strong candidates for next-generation energy storage technologies [22–27]. Capacitors are generally divided into electric double-layer capacitors (EDLCs) and pseudocapacitors, depending on how they store charge. In EDLCs, energy storage arises from the formation of an electric double layer at the electrode–electrolyte boundary, and the capacitance is directly influenced by the electrode's surface area [22–27]. In contrast, pseudocapacitors, which include metal oxide and conductive polymer-based supercapacitors, utilize fast Faradaic redox reactions, where capacitance is determined by the efficient utilization of active electrode materials [28–31]. These systems exhibit superior power density, extended lifespans, and rapid energy transfer, making them particularly suitable for high-performance energy storage applications. The performance of SCs is strongly influenced by factors such as electrode material selection, electrolyte composition, and operating conditions. Current research efforts are focused on enhancing energy density while preserving their intrinsic advantages, positioning supercapacitors as a pivotal technology in the evolving landscape of sustainable energy storage [24–31]. CMPs are a class of organic materials composed of repeating units interconnected by covalent bonds, forming a robust three-dimensional network [32–36]. Typically constructed from light elements such as carbon, nitrogen, and oxygen, CMPs exhibit diverse chemical structures, providing a wide range of tunable properties and applications [37–41]. The distinctive features of CMPs—including high surface area, adjustable porosity, and excellent chemical stability—have attracted considerable research interest in recent years [42–53]. Their intrinsic porosity facilitates efficient electrolyte penetration, while their versatile chemical composition enables enhanced charge storage capabilities. Furthermore, CMPs can be engineered to incorporate redox-active functional groups, further improving their electrochemical performance. One key advantage of CMPs in SCs applications is their exceptionally high surface area, which can be optimized through careful selection of monomers and control of molecular configuration during synthesis [2,4,14]. Various synthetic strategies have been employed to prepare CMPs, including oxidative polymerization and traditional coupling methods such as Sonogashira–Hagihara, Suzuki–Miyaura, and Yamamoto coupling reactions [33,37,38]. These approaches have enabled the production of CMPs with diverse frameworks and tailored properties. CMPs are also well-suited for electrochemical materials due to their porous architecture and extended π-conjugation, which facilitate rapid electron transport. Additionally, the presence of redox-active sites enhances their sensitivity toward target analytes. Hexaazatrinaphthalene (HATN) is an imine-based compound featuring a rigid, planar, and fully conjugated aromatic framework. While inherently electron-deficient, its extended π-conjugation and multiple imine functionalities render it an attractive building block for the design of large conjugated frameworks [54–58]. Owing to these structural characteristics, HATN-derived CMPs materials have been extensively explored as promising candidates for advanced energy storage applications [54–58]. MXenes, especially titanium carbide ($Ti_3C_2T_x$), are part of a versatile class of two-dimensional materials derived from transition-metal carbides and nitrides and have recently attracted considerable interest in electrochemical energy storage [59–61]. Their pronounced pseudocapacitive charge-storage capability, robust and highly reversible surface redox reactions in acidic electrolytes, and metal-like electronic conductivity set them apart from traditional carbon electrodes [61]. Notably, standalone MXene films with no supporting substrate have exhibited very high specific capacitance along with outstanding capacitance retention over prolonged cycling, reflecting superior electrochemical durability. These characteristics contribute to reduced charge-transfer resistance, rapid electron mobility, and improved ion/electrode interaction, enabling efficient charge exchange at the electrode–electrolyte boundary [62,63]. Altogether, these advantages highlight $Ti_3C_2T_x$ as a compelling negative electrode material for future asymmetric, high-power supercapacitor systems.

To the best of our knowledge, the rational design and construction of CMP incorporating both pyrene (PTB) and hexaazatrinaphthalene (HATN) units using Sonogashira coupling reaction and then investigating the performance of $Ti_3C_2T_x$//PTB-HATN CMP in the form of asymmetric device (ASC) has not been reported to date. The PTB–HATN CMP electrode exhibits ultra-high electrochemical charge-storage capability, achieving 1010.2 F g^{-1} at 1 A g^{-1} in 3 M H_2SO_4, and sustaining approximately 99% coulombic efficiency over repeated cycling. Beyond its high capacitance, the electrode demonstrates long-term operational endurance, preserving 97.6% of its starting capacitance after 5000 continuous charge–discharge cycles, reflecting excellent framework integrity and redox reversibility. When configured into a hybrid asymmetric supercapacitor, pairing Ti_3C_2Tx as the negative electrode with PTB–HATN CMP as the positive electrode, the full device attains a specific capacitance of 230 F g^{-1} at 1 A $g^{-1,}$ supported by well-matched charge compensation and rapid ion/electron exchange at the interface. Collectively, these results validate the hybrid system as a high-capacity and power-efficient electrode design, offering strong promise for practical next-generation supercapacitor technologies.

2. Experimental section

2.1. Materials

1,2,3,4,5,6-Cyclohexanehexone octahydrate (Cyclo-6CO), 4,6-dibromo-1,2-phenylenediamine (PH-2NH_2-2Br), potassium carbonate [K_2CO_3], triethylamine (Et_3N), acetic acid (AcOH), dimethylformamide (DMF), anhydrous magnesium sulfate ($MgSO_4$), and palladium tetrakis (triphenylphosphine) [$Pd(PPh_3)_4$], along with other required solvents, were obtained from Sigma-Aldrich. The synthesis and processing of $Ti_3C_2T_x$ were previously reported in our earlier work [61]. The compound 1,3,6,8-tetrakis(2-(trimethylsilyl)ethynyl)pyrene (PTB-MS) was synthesized according to reported procedures [64–68].

2.2. Synthesis of PTB

In a 50 mL round-bottom flask equipped with a single neck, PTB-MS (2.18 g) was combined with K_2CO_3 (4.62 g). The mixture was dissolved in methanol (40 mL) and stirred continuously at 25 °C overnight. After completion of the reaction, the mixture was diluted with distilled water (50 mL) in order to quench the reaction and to facilitate the removal of excess K_2CO_3. The resulting suspension was subjected to vacuum filtration to acquire a brown solid, and the brown solid was further purified through flash column using DCM as eluent to afford bright orange powder (PTB, 1.95 g, Yield: 89%). ^{1}H NMR [500 MHz, ppm, δ, $CHCl_3$-d, Fig. S1]: 8.68, 8.37, and 3.66 (terminal alkyne). ^{13}C NMR [125 MHz, ppm, δ, $CHCl_3$-d, Fig. S2]: 134.9, 132.5, 127.1, 117.8, 83.8 (Ph-C ≡ CH) and 81.3 (Ph-C ≡ CH).

2.3. Synthesis of HATN-6Br

A solution of PH-2NH_2-2Br, 2.0 g, 7.52 mmol, 3.0 equiv.) was prepared in AcOH (50 mL) in a 100 mL round-bottom flask. The reaction mixture was carefully degassed under a nitrogen atmosphere for 30 min to remove dissolved oxygen. Subsequently, Cyclo-6CO (783 mg, 2.51 mmol, 1.0 equiv.) was introduced under a steady reverse flow of nitrogen to maintain an inert environment. The reaction solution was then raised to its reflux temperature (110 °C) and maintained under these conditions with continuous stirring for 72 h, during which the color of the solution gradually deepened, indicating the progression of the condensation process. When the reaction was finished, the hot mixture was added dropwise onto crushed ice for efficient cooling and quenching with stirring, followed by the addition of an aqueous Na_2CO_3 solution until effervescence ceased, neutralizing the medium and promoting precipitation. The resulting solid product was collected by vacuum filtration, thoroughly washed with DMF and acetone to remove organic impurities, and the green solid was refluxed with 50 mL of HNO_3 for 1 h to afford HATN-6Br as a yellow solid [0.56 g, Yield: 74%].

2.4. Synthesis of PTB-HATN CMP

A mixture of PTB (0.45 g, 1.65 mmol) and HATN-6Br (0.294 g, 0.81 mmol) was put into a glass container containing 30 mL of DMF and 30 mL of Et_3N. The temperature of the reaction mixture increased to 115 °C and was stirred under a nitrogen atmosphere for approximately three days. After completion, the reaction was cooled to RT, resulting in the formation of a green solid, which was collected by filtration. The crude product was purified through Soxhlet extraction using THF, chloroform, methanol, and acetone in sequence. The final product, PTB-HATN CMP, was dried at 120 °C to yield fine green powder [0.39 g, Yield: 87%].

3. Results and discussion

3.1. Synthesis and characterization of PTB-HATN CMP

To construct the conjugated microporous polymer PTB-HATN CMP, two key monomeric building blocks—HATN-6Br and PTB—were first synthesized. The precursor HATN-6Br was obtained through a condensation reaction between 1,2,3,4,5,6-cyclohexanehexone octahydrate (Cyclo-6CO) and 4,6-dibromo-1,2-phenylenediamine (PH-2NH_2-2Br) in acetic acid medium [68]. The reaction afforded a yellow crystalline powder that exhibited negligible solubility in a wide range of organic solvents, suggesting its rigid and planar conjugated framework [Fig. 1(a)]. The second monomer, PTB, was synthesized by hydrolyzing PTB-MS in methanol in the presence of K_2CO_3. This process yielded an orange solid with high purity [Fig. 1(b)]. Then, the polymerization was carried out using the Sonogashira cross-coupling reaction between HATN-6Br and PTB in DMF with Et_3N as the base. The reaction proceeded smoothly to afford the target polymer PTB-HATN CMP as a green powder in good yield [Fig. 1(c)]. Notably, the as-synthesized CMP was completely insoluble in all common organic solvents, which is consistent with its high crosslinking density and confirms the successful formation of a stable porous conjugated network. The successful synthesis of HATN-6Br, PTB, and the PTB-HATN CMP framework was affirmed by Fourier transform infrared spectroscopy (FT-IR, Fig. 2(a)). The FT-IR spectrum of HATN-6Br exhibited distinct absorption bands at 3088, 1638, and 1450 cm^{-1}, which are ascribed to the characteristic vibrations of aromatic sp^2 C—H, C═N, and C═C moieties, respectively. In contrast, the PTB monomer displayed prominent absorption bands at 3282 and 2098 cm^{-1}, originating from the stretching modes of terminal alkyne C—H and C≡C bonds. Notably, the FT-IR spectrum of the PTB-HATN CMP revealed absorption features at 3069, 2185, and 1618 cm^{-1}, attributable to aromatic C—H, alkyne C≡C, and C═N functionalities, respectively. The coexistence of these diagnostic bands provides compelling evidence for the successful incorporation of HATN and PTB structural units into the PTB-HATN CMP network. The chemical stability of PTB–HATN CMP was evaluated by FT-IR spectroscopy after treatment in various solvents and chemical environments, including THF, DMF, MeOH, 1 M NaOH, and 1 M HCl (Fig. S3). All treated samples exhibited nearly identical FT-IR spectra, retaining the characteristic vibrational bands of the CMP framework, such as aromatic C—H, C≡C, and C═N stretching vibrations. No noticeable changes in peak positions or intensities were observed after exposure to organic solvents or to acidic and basic media, indicating that the chemical structure of PTB–HATN CMP remained intact. These results demonstrate the excellent chemical stability of the CMP in diverse organic solvents as well as under harsh acidic and alkaline conditions. The solid-state ^{13}C NMR spectrum of PTB-HATN CMP [Fig. 2(b)] further corroborates the successful framework formation. A resonance at ~155 ppm is assigned to the C═N units of the HATN moieties [68,69], while multiple signals spanning 141–119 ppm are characteristic of aromatic carbons originating from both the HATN and PTB units. Additionally, distinct resonances at 92 and 82 ppm are associated with the alkyne C≡C carbons of the PTB segments, unequivocally confirming the preservation of alkyne functionalities within the CMP backbone. XRD analysis demonstrated that HATN-3Br (Fig. S4) and PTB (Fig. S5) are crystalline materials, while PTB–HATN CMP displays an amorphous nature (Fig. S6), in agreement with the typical structural features of CMPs reported in the literature [69,70]. X-ray photoelectron spectroscopy (XPS) analysis (Fig. S7) provided further insights into the elemental composition and electronic environment of PTB-HATN CMP. The survey spectrum confirmed the presence of carbon (C 1 s, 283.8 eV) and nitrogen (N 1 s, 398 eV) as the principal constituents of the framework.

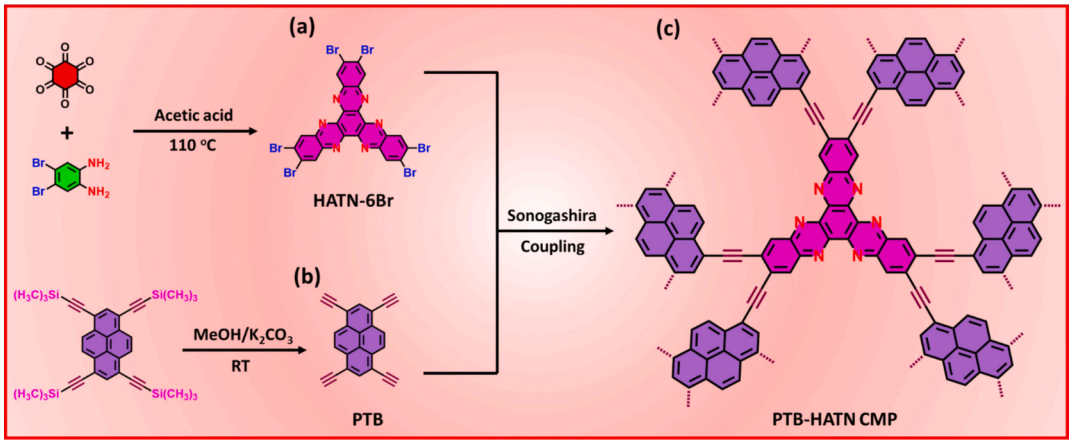

Fig. 1. Schematic representation of the preparation of (a) HATN-6Br, (b) PTB, and (c) PTB-HATN CMP.

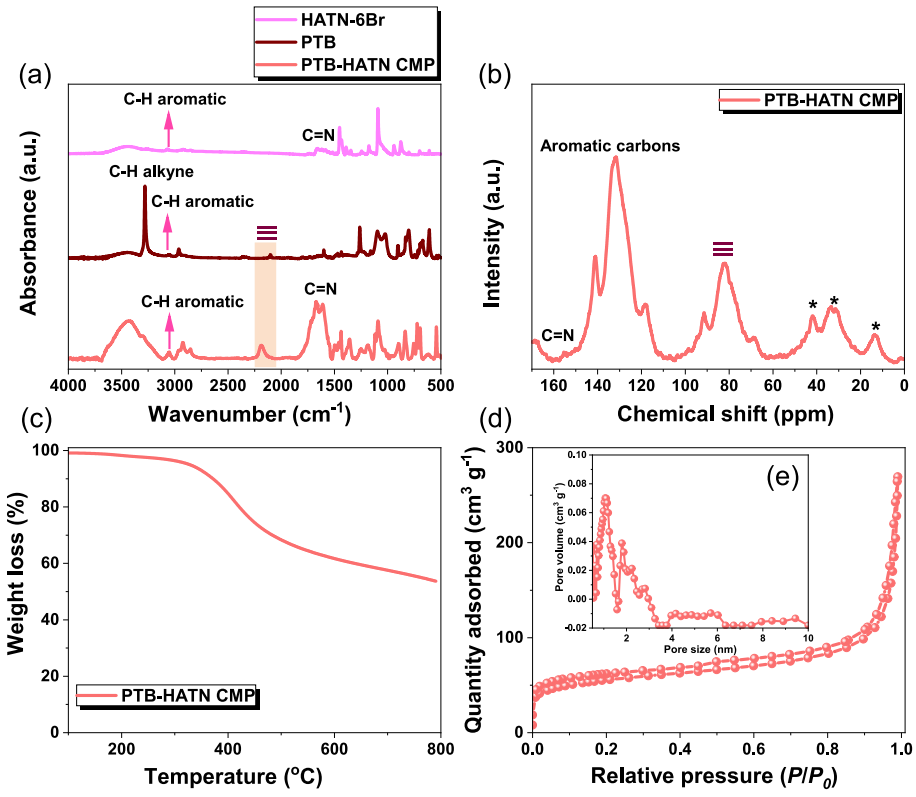

Fig. 2. (a) FTIR spectra of HATN-6Br, PTB, and PTB-HATN CMP, (b) solid-state ^{13}C NMR, (c) TGA, (d) N_2 adsorption–desorption isotherms, and (e) pore size distribution of PTB-HATN CMP.

Deconvolution of the high-resolution C 1 s spectrum revealed distinct peaks at 285.5, 284.5, and 283.5 eV, corresponding to C═N, C≡C, and C–C/C=C bonds, respectively [54]. In the N 1 s region, a pronounced peak at 398 eV was observed, which is attributed to the C═N functionalities of the HATN units, thereby substantiating the successful incorporation of nitrogen-rich moieties into the CMP backbone [54,69,70]. As depicted in [Fig. 2(c)], thermogravimetric analysis (TGA) revealed that PTB-HATN CMP recorded under an inert atmosphere possesses remarkable thermal stability, exhibiting only 10% weight loss from room temperature to 360 °C. When further increasing the temperature, up to 800 °C, PTB-HATN CMP retained 53 wt%. This phenomenon strongly reveals that intrinsic robustness and enhanced thermal resistance are imparted by the HATN-linked conjugated framework. No melting peak was observed in the DSC thermogram of PTB–HATN CMP [Fig. S8], indicating that the material is amorphous rather than crystalline. The nitrogen adsorption–desorption isotherm of PTB-HATN CMP [Fig. 2(d)] can be classified as Type II according to IUPAC standards, characterized by a pronounced hysteresis loop. The isotherm displays a gradual uptake at low relative pressures, indicative of micropore filling, followed by a sharp increase at higher pressures, consistent with the presence of mesoporous domains. The BET surface area of PTB-HATN CMP is 198 $m^2\ g^{-1,}$ along with a pore volume of 0.41 $cm^3\ g^{-1}$. Moreover, the desorption branch hysteresis loop reveals the formation of interconnected pore channels, with pore size distribution analysis (non-local density functional theory, NLDFT model) revealing distinct pore diameters of 1.1, 1.8, 2.3, and 2.9 nm, respectively, for PTB-HATN CMP [Fig. 2(e)]. Therefore, the presence of a microporous network in PTB-HATN CMP facilitates rapid ion diffusion pathways and enhances rapid ion transport. Therefore, the increased surface area offered by PTB-HATN CMP promotes greater interaction with electrolyte ions, thereby improving rapid ion diffusion. Scanning electron microscopy (SEM) images [Figs. 3(a) and 3(b)] revealed that PTB-HATN CMP adopts an aggregated nanosphere morphology interconnected with thin sheet-like structures. Elemental mapping from SEM-EDS confirmed the uniform distribution of carbon [red color, Fig. 3(c)] and nitrogen [green color, Fig. 3(d)] throughout the framework, consistent with the expected composition. Transmission electron microscopy (TEM) further corroborated these observations, clearly displaying the nanosphere architecture [Figs. 3(e) and 3(f)], in excellent agreement with the SEM results.

3.2. *Electrochemical performance of the PTB–HATN CMP as positive electrode in a three-electrode configuration*

To investigate the pseudocapacitive charge storage mechanism of PTB-HATN CMP, electrochemical measurements were first conducted in a conventional three-electrode system. The working electrode was fabricated by coating PTB-HATN CMP in the form of slurry onto graphite foil, while a platinum wire was employed as the counter electrode, and an Ag/AgCl electrode functioned as the reference electrode, respectively. Electrochemical performance was evaluated in 3 M H_2SO_4 electrolyte using cyclic voltammetry (CV) and galvanostatic charge–discharge (GCD) measurements. The CV curves of PTB-HATN CMP electrode [Fig. 4(a)] revealed two pairs of well-defined and reversible redox peaks, with anodic potentials at $Epa_1 = 0.33$ V and $Epa_2 = 0.46$ V, and corresponding cathodic potentials at $Epc_1 = 0.37$ V and $Epc_2 = 0.226$ V. These redox features within the potential window between 0 to +0.7 V, can be ascribed to the electroactive pyrene moieties covalently integrated into the CMP framework. On the other hand, PTB-HATN CMP also exhibited two reversible redox peaks in 3 M KOH [Fig. S9], however, the peak positions are located at negative regions $Epa_1 = -0.62$ and $Epa_2 = -0.83$ V, and the corresponding cathodic peak potentials at $Epc_1 = -0.71$ V and $Epc_2 = -1.0$ V, respectively. Based on the comparison between acidic and basic electrolytes, it can be revealed that the electrochemical performance of PTB-HATN CMP is highly dependent on pH. Taking into consideration the stronger redox peaks located at acidic electrolyte when compared with basic electrolyte, the electrochemical performance for PTB-HATN CMP electrode in the present work was carried out using 3 M H_2SO_4 only. When pyrene-based molecules

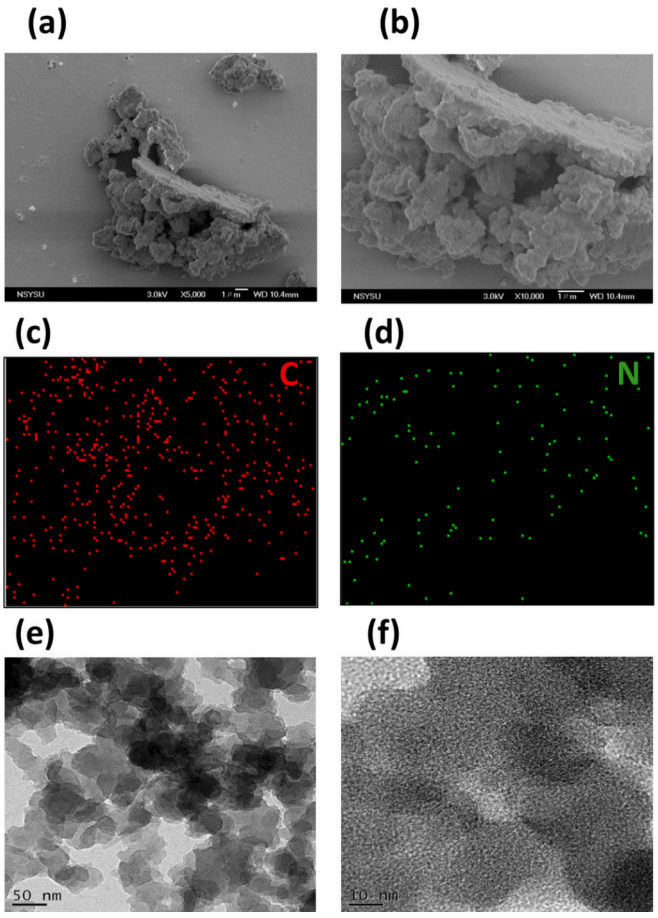

Fig. 3. (a, b) SEM, (c, d) SEM-EDS mapping, and (e, f) TEM images of PTB-HATN CMP.

are coated on an electrode and placed in an acidic medium, they undergo an electrophilic substitution reaction and generate -OH group on (C4). To compensate for the stability of the resultant structure, the -OH group can also be generated on the (C9) position of the pyrene present in PTB-HATN CMP. Owing to the passivation of electrolyte ions, the wettability of the electrode is affected, and dihydroxypyrene is generated. When subjected to continuous cycles, the formed dihydroxypyrene undergoes a two-electron and two-proton process, resulting in the reversible formation of pyrene quinones [Scheme S1], which reveals the electrochemical oxidation of pyrene in an acidic medium [71]. Two reversible redox peaks emerge within the potential window of 0–0.7 V, reflecting the underlying process described above.

Moreover, at higher scan rates from 2 to 100 mV s^{-1} in the same potential range, the CV profiles consistently retain the two reversible redox processes. The retention of reversible process at all scan rates indicates that the charge storage in PTB-HATN CMP arises from a synergistic combination of EDLC and pseudocapacitance. Herein, EDLC behavior is due to the presence of a microporous carbon network that allows ion adsorption/desorption behavior at the electrode–electrolyte interface, and the observation of pseudocapacitive behavior has mainly arisen from the formation of pyrene quinones that favor reversible redox reaction. The overall capacitance of the PTB-HATN CMP electrode can be attributed to two primary contributions: (i) fast faradaic redox reactions occurring at surface or near-surface active sites, and (ii) electrostatic charge storage via ion adsorption/desorption. A smaller fraction originates from ion diffusion within the bulk of the electrode material. It is important to highlight that the redox peaks of PTB-HATN CMP were still retained at 100 mV s^{-1}, demonstrating excellent rate capability and structural stability under high scan rate conditions. Based on CV measurements, the specific capacitances of PTB-HATN CMP were determined to be 250, 234, 221, 205, 197, 190, 186, 181, 177, 174, 170, and 167 F g^{-1} at 2, 5, 10, 20, 30, 40, 50, 60, 70, 80, 90, and 100 mV s^{-1}, respectively [Fig. 4(b)]. The specific capacitance was well-retained even at high scan rates, further revealing that the inherent high surface area of CMPs arises from their micropores. As illustrated in the CV response, the PTB-HATN CMP electrode with high mass loading also exhibited redox response in the presence of 3 M H_2SO_4 [Fig. S10(a)]. However, the observation of redox behavior is distinct evidence of the high mass loading of PTB-HATN CMP on the surface of graphite foil. This might be due to the presence of limited diffusion pathways, which restricted the ionic transport and thus well-resolved peaks are not distinctly observed. When subjected to GCD experiments with current densities of 1, 2, 3, 4, 5, 7, and 10 A g^{-1} [Fig. S10(b)], the specific capacitance was calculated to be 108.4 F g^{-1} at 1 A g^{-1} and reached 58.4 F g^{-1} at 10 A g^{-1} [Fig. S10 (c)].

To better clarify the charge storage behavior, Cottrell's equation ($I \propto v^{0.5}$) was employed. The linear dependence of the redox peak current (I) on the scan rate confirmed the coexistence of both surface-confined pseudocapacitance and EDLC in PTB-HATN CMP [Fig. 4(c)]. To assess and compare the relative influence of surface-controlled versus diffusion-controlled processes, the Trasatti method was applied. This approach enables the separation of the surface-accessible charge (Q_{outer}) from the total stored charge (Q_{total}), thereby providing a deeper understanding of the energy storage mechanism in PTB-HATN CMP: $Q = Q_{outer} + Kv^{0.5}$, where Q is the charge (C g^{-1}) at a specific scan rate (v), and K is a constant, we identified the contribution from surface processes. This approach complements the kinetic analysis and provides a more comprehensive understanding of the storage mechanism. Additionally, the electrode kinetics were further analyzed using the power-law relationship ($i = av^b$), where i is the current, v is the scan rate, and a and b are adjustable parameters. The b-value was obtained from the slope of the log(i) versus log(v) plot. The b-value approaching 1 indicates a capacitive-controlled process, whereas a value close to 0.5 suggests diffusion-limited behavior. For the PTB-HATN CMP electrode, b-values of 0.84 (cathodic process) and 0.91 (anodic process) were determined, confirming that the charge storage is predominantly capacitive in nature [Fig. 4(d)]. In addition, the linear relationship between i and v was examined using the Randles–Ševčík equation. The observed proportionality between scan rate and peak current further demonstrates that the charge storage is governed primarily by adsorption-controlled processes [Fig. 4(c)]. To further separate the capacitive and diffusive contributions, the current response at each scan rate Fig. 4(e)] was analyzed using the Dunn Model equation:

$$i(V) = k_1 v + k_2 v^{1/2}.$$

In this model, $k_1 v$ represents the capacitive (surface-controlled) contribution, while $k_2 v^{1/2}$ represents the diffusion-controlled part. By applying this method, the relative percentages of both contributions were calculated at 100 mV s^{-1} [Fig. 4(f)], the capacitive contribution markedly increased to 88.8%, accompanied by a decrease in the diffusion-controlled portion to 11.17%. These findings confirm that PTB-HATN CMP predominantly stores charge through rapid surface-controlled processes. Dunn's analysis further illustrates the relative contributions of capacitive and diffusion effects at both low and high scan rates. The PTB-HATN CMP electrode exhibited a capacitance contribution of about 53% at 2 mV s^{-1} and reached 89% at 100 mV s^{-1}, whereas the diffusive contribution was calculated to be 47% at 2 mV s^{-1} and reached 11% at 100 mVs^{-1}, indicating the overall electrochemical process is dominated by a capacitive-controlled process. For a more comprehensive assessment of the electrode's electrochemical capability, GCD analysis was conducted within 0 to 0.7 V, with stepwise current densities from 1–5 A g^{-1}. As revealed from [Fig. 5(a)], GCD profiles exhibited non-linear triangular shapes with distinct redox features, consistent with the CV results. The PTB-HATN CMP electrode delivered

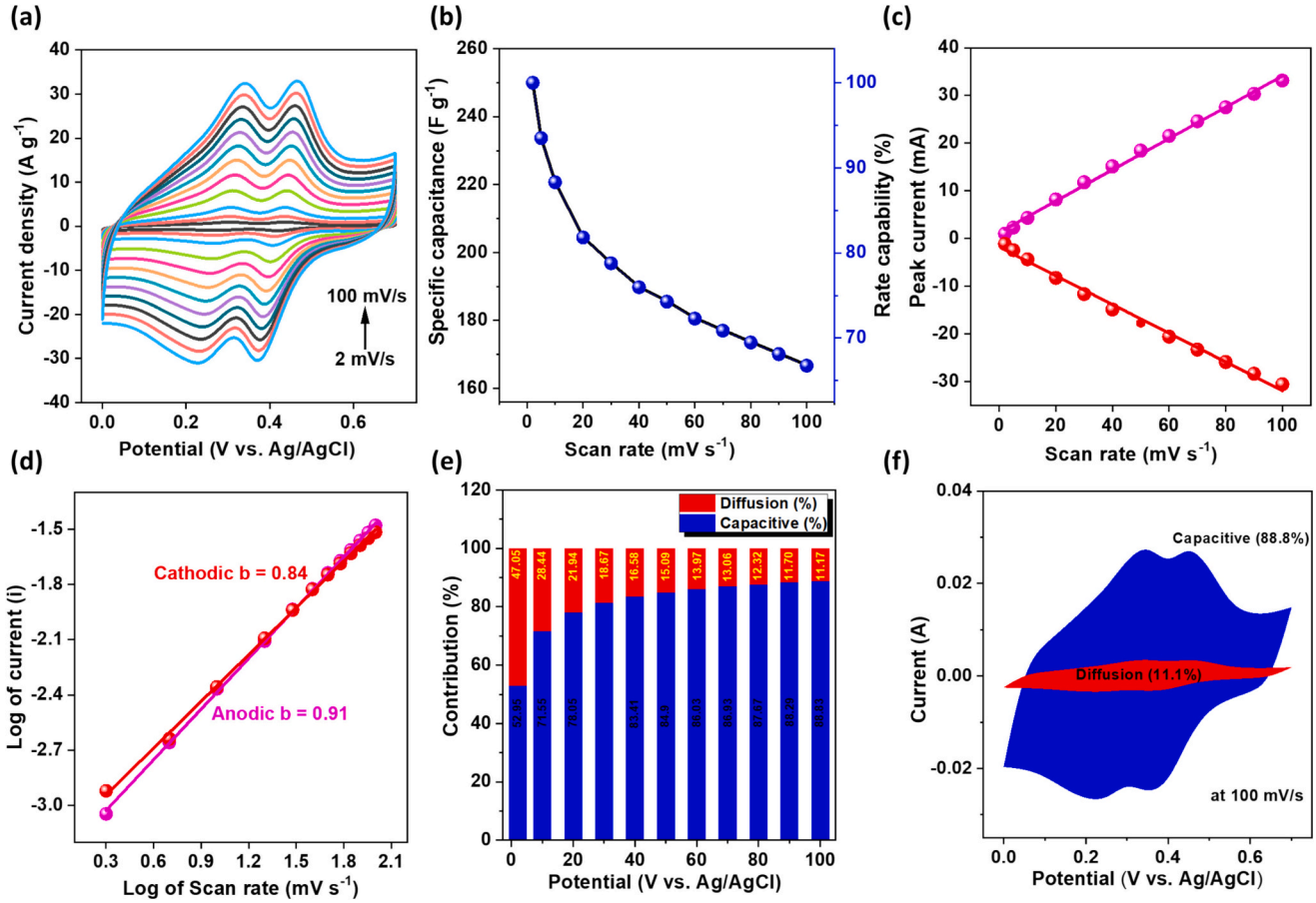

Fig. 4. (a) CV curves of Py-HATN CMP electrode at different scan rates [recorded in presence of 3 M H_2SO_4], (b) Specific capacitance from CV for various scan rate, (c) linear dependence between current as a function of scan rate, (d) evaluation of b-value from log of scan rate vs log of I, and (e) effect of charge storage contribution at various scan rate and (f) charge storage contribution obtained using Dunn Model at 100 mV s^{-1}.

a high SC of 1010.2 F g^{-1} at 1 A g^{-1}, which decreased to 315 F g^{-1} at 5 A g^{-1}, reflecting rate-dependent behavior [Fig. 5(b)]. The observation of high-rate capability offered by the PTB-HATN CMP electrode is mainly due to the formation of pyrene quinone (which enables redox functionality) and the presence of a large surface area, which reduces the ion transport pathways, leading to accommodation of abundant ions for efficient ion storage. As shown in Table S1, the PTB–HATN CMP-based supercapacitors (SCs) operating in a three-electrode configuration exhibit a remarkably high SC [1010.2 F g^{-1} @1 A g^{-1}], which surpasses the performance of most previously reported CMP electrodes. Electrochemical impedance spectroscopy (EIS) is a powerful tool to investigate the charge-transfer resistance (R_{ct}) and cycling stability of the PTB–HATN CMP electrode before and after prolonged cycling. The corresponding Nyquist plots are shown in Fig. 5(c), where the real (Z′) and imaginary (Z″) components of impedance are plotted along the x- and y-axes, respectively. The observation of a small semicircle in the high-frequency range for both electrodes represents the smaller R_{ct} at the electrode/electrolyte interface. In detail, the PTB-HATN CMP electrode recorded before cycling exhibits a low R_{ct} value of approximately 1.01 Ω, indicating that the presence of conjugated π bonds in CMPs favors electron transport pathways, leading to excellent conductivity.

On the other hand, the resultant PTB-HATN CMP electrode obtained after 5000 cycles retained a similar response at higher frequencies without any significant change in the R_{ct} value (0.904 Ω) [Table S2], indicating good stability of the electrode; however, the deviation was observed at lower frequencies. Overall, EIS results confirm that PTB-HATN CMP possesses low resistance, good electronic conductivity, and excellent cycling stability. Notably, after 5000 continuous charge–discharge cycles, the electrode retained robust performance, highlighting its potential as a durable electrode material for long-life supercapacitors. The four-point probe method was used to determine the electrical characteristics of PTB-HATN CMP by measuring sheet resistance and volume resistivity, and electrical conductivity while maintaining low contact resistance. The graph in Fig. S11 displays the correlation between the measured resistance (Ω) and the corresponding sheet resistance (Ω/sq) for PTB-HATN CMP. From the graph, it can be appreciated that the sheet resistance increases monotonically with the measured resistance. The monotonic rise in the sheet resistance with the measured resistance implies a uniform charge transport mechanism over the entire surface. At values of resistance <4.4 Ω and > 3.9 Ω, the sheet resistance is found to lie within a narrow range of ≈17–19 Ω/sq. At higher values of resistance <9.4 Ω, the sheet resistance has a value ≈41.7 Ω/sq. The measured volume resistivity shows values between 0.93 and 2.19 Ω·cm, while the electrical conductivity shows a decrease from 1.08 to 0.46 S·cm^{-1}. The direct relationship between resistivity and conductivity demonstrates that four-point probe measurements produce consistent and accurate results. The resistance–sheet resistance relationship shows a linear and systematic pattern, which confirms that PTB-HATN CMP maintains material uniformity and consistent electrical properties. To evaluate the stability of the CMPs, the resultant PTB-HATN CMP was subjected to cycling stability at 7 A g^{-1}. As depicted in Fig. 5(d), following 5000 cycles of continuous testing, the PTB-HATN CMP electrode delivered sustained capacitive performance, retaining 97.6% of its original electrochemical response with negligible stability loss. The observation of higher capacitive retention for CMP signifies that the formation of pyrene quinone generates stable, reversible redox

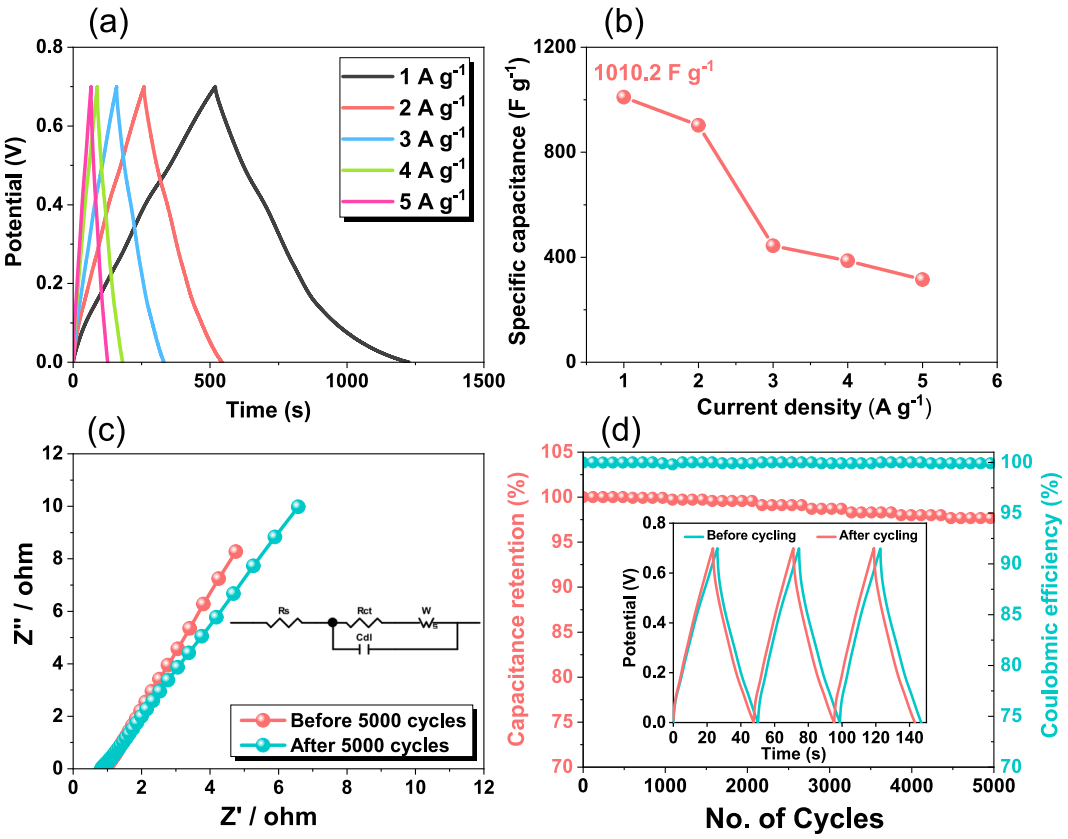

Fig. 5. (a) GCD curves of PTB-HATN CMP electrode recorded in the presence of 3 M H_2SO_4 at various current densities, (b) specific capacitance calculated from GCD curves with respect to current density, (c) EIS curves of PTB-HATN CMP electrode before and after being subjected to 5000 cycles [Inset: the equivalent circuit for the PTB-HATN CMP electrode] and (d) stability of PTB-HATN CMP electrode for a period of 5000 cycles.

peaks, and therefore, the degradation of CMPs is minimal. In addition, the coulombic efficiency remained close to 99% throughout all the cycles, confirming the highly reversible and efficient nature of the charge–discharge process. Inset Fig. 5(d) compares the GCD curves for PTB-HATN CMP before and after 5000 cycles, showing only a slight decrease in discharge time after extended cycling, further revealing the retention of CMPs without any degradation even when subjected to prolonged cycles.

3.3. Post analysis of PTB-HATN CMP electrode

FT-IR spectroscopy was employed as a primary tool to examine the structural evolution of PTB-HATN CMP, particularly the transformation of pyrene terminal units into pyrene quinone during electrochemical cycling. The FT-IR spectra of PTB-HATN CMP after 2000 and 5000 cycles in 3 M H_2SO_4 are presented in Fig. S12 (ex-situ analysis). Before cycling, no broad bands associated with –OH stretching vibrations were observed in the 3500–3000 cm^{-1} region, confirming that the pristine PTB-HATN CMP contains no hydroxyl groups. After 2000 cycles, a broad absorption band emerged in this region, indicating the formation of hydroxyl-functionalized pyrene units. Upon further cycling to 5000 cycles, the intensity of this band increased, accompanied by the appearance of a strong peak near 1650 cm^{-1}, which corresponds to C═O stretching. These observations collectively confirm the generation of –OH and C═O functionalities, consistent with the formation of hydroxy-pyrene and pyrene-quinone species during repeated redox processes. SEM analysis was carried out to evaluate morphological changes in the electrodes before and after 5000 continuous cycles. The pristine PTB-HATN CMP electrode displays well-distributed active material embedded within the carbon binder matrix, with clearly visible spherical CMP particles at higher magnification. Notably, similar spherical morphologies were retained even after extended cycling in 3 M H_2SO_4, indicating that the CMP framework remains intact and does not suffer from structural degradation. Furthermore, the electrode surface exhibited no visible cracks after cycling, suggesting excellent mechanical stability [Fig. S13]. These features reflect that electrode packing density prevents the electrode from cracking and thus the ionic transport pathway is facilitated even after subjected to continuous cycles. XPS analysis was employed to gain further insight into the oxidation states and chemical transformations associated with pyrene units during cycling. The survey spectrum of the electrode after 5000 cycles revealed signals corresponding to C, N, O, and S, consistent with the expected elemental composition [Fig. S14]. The high-resolution C 1 s spectrum was deconvoluted into four components at 284.7 eV, 286.4 eV, 288.4 eV, and 291.4 eV, assigned to C–C/C=C, C=N/C–OH, C═O, and CF_2, respectively. The presence of C–OH and C═O peaks confirms the formation of hydroxypyrene and pyrene-quinone species. The CF_2 peak originates from the PVDF binder. Similarly, the N 1 s spectrum was deconvoluted into peaks at 400.7 eV and 402.9 eV, corresponding to C═N and C—N groups in the PTB-HATN CMP framework. The O 1 s region displayed two peaks at 534.79 eV (O=C) and 533.07 eV (H–O–C). Solid-state ^{13}C NMR spectroscopy was carried out for PTB-HATN CMP after 5000 cycles. The spectrum clearly shows the presence of the C═O carbon signal at approximately 179.2 ppm, confirming the retention of the carbonyl functional group [Fig. S15]. FTIR, XPS, and solid-state ^{13}C NMR results collectively revealed the formation of hydroxypyrene and pyrenequione during charging and discharging cycles.

3.4. Electrochemical performance of $Ti_3C_2T_x$ free-standing film as a negative electrode

As is evident with the formation of pseudocapacitive behavior for

PTB-HATN CMP for the positive electrode, choosing the negative electrode, which also possesses pseudocapacitive behavior, is highly preferable when compared with conventional carbon-based electrodes (EDLC behavior). Based on the literature, $Ti_3C_2T_x$ obtained from Ti_3AlC_2 (MAX) is reported to exhibit high pseudocapacitance. Therefore, the preparation of free-standing $Ti_3C_2T_x$ film was adopted from our previously reported work [61]. In brief, Ti_3AlC_2 was subjected to the selective etching of Al using LiF and HCl (MILD method), followed by washing with double-distilled water until the supernatant became dark green. The resultant swelled m-$Ti_3C_2T_x$ was delaminated using LiCl to obtain dark supernatants, which are named as single-layered MXene nanosheets. The free-standing $Ti_3C_2T_x$ film was obtained after vacuum-assisted filtration [61]. The electrochemical performance of $Ti_3C_2T_x$ film was recorded in the presence of 3 M H_2SO_4 and exhibited redox peaks with the observation of $Epa = -0.153$ V and $Epc = -0.301$ V within the potential window from 0.3 to −0.5 V [Fig. 6(a)]. Herein, the observation of redox reaction between excessive protons in acidic electrolyte (3 M H_2SO_4) and surface functionalized (-OH, -F) $Ti_3C_2T_x$ film facilitates the oxidation of Ti into $Ti_3C_2O_x$. Based on the CV with redox response for $Ti_3C_2T_x$ film, which evidences the pseudocapacitive behavior, and in order to estimate the rate capability, scanning within the same potential window at different scan rates was performed. As evident from Fig. 6(b), the redox peak currents were found to increase with an increase in the scan rate from 5 mV s^{-1} to 100 mV s^{-1}. Moreover, the redox behavior was clearly visualized even at higher scan rates, which clearly signifies the $Ti_3C_2T_x$ film with good rate capability. As we successfully evaluated the kinetic behavior of the positive electrode, the electrode kinetics for the negative electrode were also adopted. By implementing the power law $i = av^b$, a linear relationship was plotted between log(i) versus log(v). The resultant slope value b was calculated to be 0.96 and 0.9 for anodic and cathodic segments, respectively [Fig. 6 (c)]. These values clearly depict that the electrochemical charge storage for the $Ti_3C_2T_x$ film is predominantly capacitive in nature. In addition, the contribution to the $Ti_3C_2T_x$ film is highly dominated by capacitive behavior of about 73 and 89% at 10 and 100 mV s^{-1}, respectively [Fig. 6 (d)]. These findings observed for the $Ti_3C_2T_x$ film strongly demonstrated the pseudocapacitive electrochemical process. Furthermore, to evaluate the specific capacitance of $Ti_3C_2T_x$ film, GCD experiments [Fig. 6(e)] were performed at various current densities [ranging from 1 to 10 A g^{-1}]. The GCD curves were found to be symmetrical within the applied potential window, ranging from -0.4 to 0.3 V, during both charging and discharging. Moreover, the specific capacitance was calculated to be 173.2 F g^{-1} at 1 A g^{-1} [Fig. 6(f)].

3.5. *Electrochemical performance of all pseudocapacitive $Ti_3C_2T_x$//PTB-HATN CMP asymmetric device*

For practical validation, an asymmetric pseudocapacitive supercapacitor cell (ASC) was fabricated, employing PTB-HATN CMP as the positive electrode and $Ti_3C_2T_x$ film as the negative electrode, separated by Whatman filter paper in a Swagelok cell configuration. The use of pseudocapacitive materials for both electrodes is particularly advantageous, as the redox activity of both the positive and negative electrodes significantly enhances the overall charge storage capability of the device. To determine the optimal operating voltage window of the ASC, electrochemical measurements were conducted across various potential

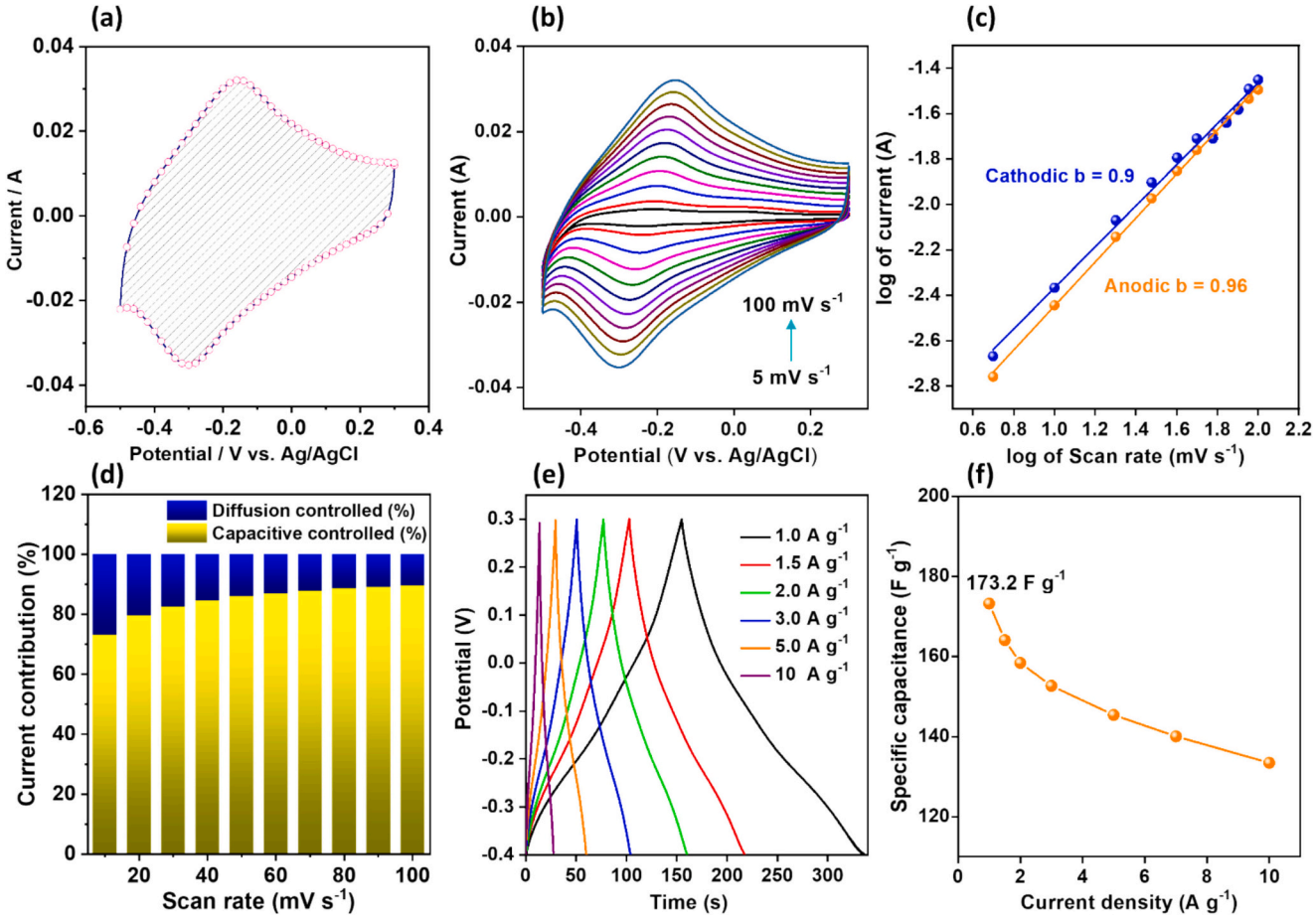

Fig. 6. (a) CV response for Ti_3C_2 film recorded in the presence of 3 M H_2SO_4 at a scan rate of 100 mV s^{-1}. (b) CV profiles of Ti_3C_2 film at various scan rates ranging from 5 mV s^{-1} to 100 mV s^{-1}. (c) Logarithmic plot between scan rate vs anodic/cathodic peak current. (d) Effect of contribution, (e) GCD profiles for Ti_3C_2 film at various current densities, and (f) specific capacitance obtained at various current densities.

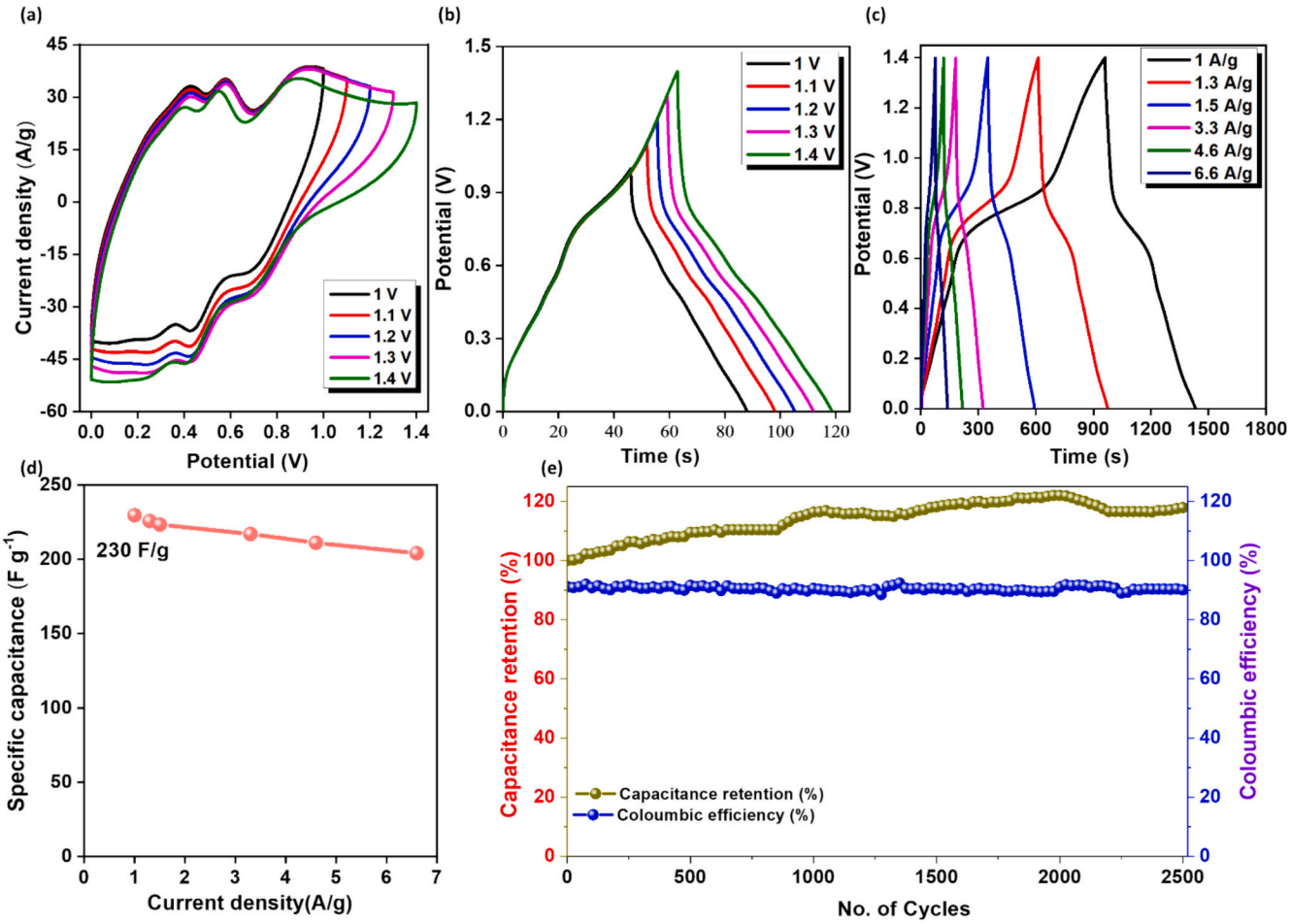

Fig. 7. (a) CV of the $Ti_3C_2T_x$//PTB-HATN CMP asymmetric cell configuration at various potentials [1-1.4 V] (b) galvanostatic charge/discharge profile of the PTB-HATN CMP in ASC at various potentials (c) GCD profile of $Ti_3C_2T_x$//PTB-HATN CMP ASC at various current density, (d) specific capacitance of $Ti_3C_2T_x$//PTB-HATN CMP asymmetric cell, and (e) cyclic stability of fabricated device over 2500 cycles.

ranges. The device exhibited a wide and stable potential window of up to 1.4 V without noticeable side reactions [Fig. 7(a)]. Furthermore, the CV profiles of the ASC displayed distinct redox peaks, confirming the active contribution of both PTB-HATN CMP and $Ti_3C_2T_x$ to the charge storage process. To further optimize the operating potential window, GCD measurements were conducted at voltages up to 1.4 V under constant current conditions [Fig. 7(b)]. No evidence of side reactions was observed, confirming the electrochemical stability of the ASC within this potential range. The GCD curves, recorded at current densities between 1 and 6.6 A g^{-1} [Fig. 7(c)], exhibited quasi-triangular profiles with slight deviations, reflecting the coexistence of EDLC and pseudocapacitive behavior. At a 1 A g^{-1}, the $Ti_3C_2T_x$//PTB-HATN CMP electrode delivered a specific capacitance of 230 F g^{-1} [Fig. 7(d)]. This value is notably higher than that of the other CMP-based electrodes, most likely due to its relatively larger BET surface area, which facilitates more efficient transport and accessibility to active sites. At a higher 6.6 A g^{-1}, the capacitance decreased to 204 F g^{-1}.

Such a decline is typical, as higher current densities shorten the ion diffusion time, thereby reducing access to electroactive sites and lowering the effective capacitance. The fabricated asymmetric pseudocapacitive $Ti_3C_2T_x$//PTB-HATN CMP device delivers a high energy density of 62.5 Wh kg^{-1} at a power density of 467 W kg^{-1}, and maintains 55.5 Wh kg^{-1} even at an elevated power density of 3.1 kW kg^{-1} [Fig. S16]. Notably, the device sustains competitive energy storage at fast charge–discharge rates without sacrificing energy density, highlighting its suitability for long-term, high-rate operation. This performance is attributed to the synergistic combination of ion intercalation within the MXene layers and the reversible surface redox activity of the phenazine-rich CMP, which together promote rapid ion diffusion, efficient charge transfer, and stable electrochemical kinetics. The sustained high-rate energy retention demonstrates that the synthesized PTB-HATN CMP is a promising electrode material for durable energy-storage systems and long-term practical applications. The cycling stability of the fabricated ASC was further examined over 2500 continuous charge–discharge cycles [Fig. 7(e)], providing insight into its long-term performance. As shown in Fig. 7(e), the ASC retained approximately 117.8% of its initial capacitance after 2500 continuous cycles. The gradual increase in capacitance during cycling suggests that the presence of a layered structure of MXene nanosheets could accommodate a large number of H^+ ions at the negative electrode, leading to enhanced utilization of the active material. These results demonstrate the robustness of the ASC, with minimal loss in energy storage capability even after extended operation, highlighting its suitability for durable supercapacitor applications. Furthermore, the coulombic efficiency remained consistently close to 90%, indicating highly reversible and efficient charge–discharge processes, where nearly all the input energy is recoverable. Overall, the PTB-HATN CMP electrode exhibits excellent cycling stability and high efficiency, underscoring its potential as a reliable and high-performance material for advanced energy storage devices. The electrochemical performance of PTB-HATN CMP is strongly governed by its intrinsic electronic structure and its synergistic interaction with the conductive MXene framework. To elucidate this relationship, molecular electrostatic potential (MESP) and frontier molecular orbital analyses were employed as qualitative electronic

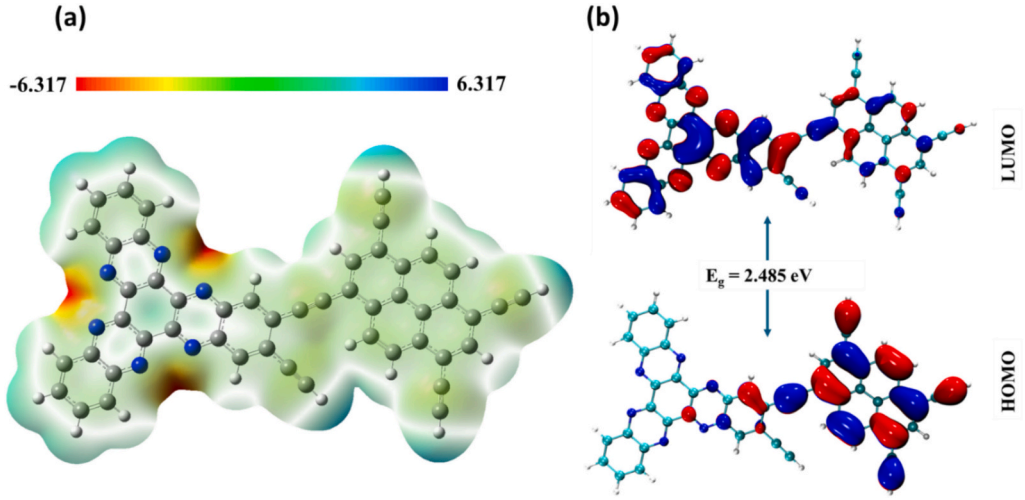

Fig. 8. (a) The MESP map and (b) the HOMO-LUMO orbitals of PTB-HATN CMP.

descriptors of charge distribution, redox activity, and charge-transport pathways. As shown in Fig. 8(a), the MESP map reveals pronounced electron-rich regions localized around the triazine- and pyrazine-type nitrogen atoms of the HATN units. These nitrogen centers act as primary redox-active sites, facilitating reversible faradaic reactions during electrochemical cycling. In parallel, a moderately electron-dense region extends across the π-conjugated backbone, indicating effective intramolecular charge delocalization. This dual distribution of localized redox centers and delocalized conjugation enables efficient charge accumulation while maintaining electronic continuity throughout the PTB-HATN CMP framework. Frontier molecular orbital analysis [Fig. 8 (b)] provides further mechanistic insight. The highest occupied molecular orbital (HOMO) is predominantly localized on the nitrogen-rich moieties, confirming their direct involvement in oxidation-reduction processes during the charging step. In contrast, the lowest unoccupied molecular orbital (LUMO) exhibits a highly delocalized distribution over the extended conjugated skeleton, providing continuous electron-accepting pathways during discharge. Such spatial separation of redox-active donor sites and delocalized electron-transport channels is favorable for rapid charge-transfer kinetics. Notably, the relatively narrow HOMO-LUMO energy gap (E_g = 2.485 eV) indicates enhanced intrinsic electronic conductivity. This reduced energy barrier facilitates efficient electron migration within the PTB-HATN CMP network and supports fast intramolecular charge transport. When PTB–HATN CMP is integrated with Ti_3C_2Tx, the highly conductive MXene sheets function as electron highways, effectively wiring the redox-active CMP domains to the current collector and minimizing interfacial charge-transfer resistance. This electronic synergy between the CMP's redox-active, nitrogen-rich framework and the metallic conductivity of MXene provides a clear mechanistic basis for the experimentally observed low charge-transfer resistance, high-rate capability, and excellent cycling stability. Consequently, the combined theoretical and electrochemical analyses demonstrate that the high performance of the $Ti_3C_2T_x$//PTB-HATN CMP originates from accelerated surface-controlled redox reactions coupled with rapid electronic transmission across the hybrid interface.

4. Conclusions

Herein, we synthesized PTB-HATN CMP, a newly developed CMP synthesized via Sonogashira coupling of PTB and HATN-derived monomers. The PTB-HATN CMP features exceptional thermal stability, robust structural integrity, and a microporous architecture with a high BET surface area (198 $m^2\ g^{-1}$). These characteristics endow PTB-HATN CMP with excellent electrochemical properties, including a specific capacitance (SC) of 1010.2 F g^{-1} at 1 A g^{-1} and long-term durability (after 5000 cycles) in an acidic electrolyte. Importantly, in an asymmetric supercapacitor configuration pairing $Ti_3C_2T_x$ (negative electrode) with PTB–HATN CMP (positive electrode), as a $Ti_3C_2T_x$// PTB–HATN CMP asymmetric cell, the asymmetric supercapacitor delivered 230 F g^{-1} at 1 A g^{-1}. The efficient charge balance and rapid ion/electron transport across the hybrid interface demonstrate both high storage capacity and strong power capability due to high-rate charge transfer between electrolyte ions and the redox active surface of the CMP electrode and MXene, supporting its promise as a practical electrode design for next-generation supercapacitors.

CRediT authorship contribution statement

Mohamed Gamal Mohamed: Writing – review & editing, Writing – original draft, Supervision, Methodology, Investigation, Formal analysis, Data curation, Conceptualization. **Poonam Nagendra Singh:** Data curation, Conceptualization. **Elangovan Sivasurya:** Writing – original draft, Formal analysis, Data curation. **Reeba Mary Mammen:** Data curation. **Hira Karim:** Software. **Ahmed F. Saber:** Data curation. **Pramod K. Kalambate:** Formal analysis. **Devaraj Manoj:** Writing – review & editing, Writing – original draft, Supervision, Resources. **Da-Ren Hang:** Supervision. **Shiao-Wei Kuo:** Supervision, Resources.

Declaration of competing interest

The authors declare that they have no known competing financial interests or personal relationships that could have appeared to influence the work reported in this paper.

Acknowledgments

This study was supported financially by the National Science and Technology Council, Taiwan, under contracts NSTC 113-2223-E-110-001 and 113-2221-E-110-012-MY3. The authors thank the staff at National Sun Yat-sen University for their assistance with the TEM.

Appendix A. Supplementary data

Supplementary data to this article can be found online at https://doi.org/10.1016/j.est.2026.121234.

Data availability

Data will be made available on request.

References

[1] J.R. Miller, P. Simon, Electrochemical capacitors for energy management, Science 321 (2008) 651–652, https://doi.org/10.1126/science.1158736.

[2] M.G. Mohamed, S.Y. Chang, M. Ejaz, M.M. Samy, A.O. Mousa, S.W. Kuo, Design and synthesis of bisulfone-linked two-dimensional conjugated microporous polymers for CO_2 adsorption and energy storage, Molecules 28 (2023) 3234, https://doi.org/10.3390/molecules28073234.

[3] Y. Zhu, S. Murali, M.D. Stoller, K.J. Ganesh, W. Cai, P.J. Ferreira, A. Pirkle, R. M. Wallace, K.A. Cychosz, M. Thommes, D. Su, E.A. Stach, R.S. Ruoff, Carbon-based supercapacitors produced by activation of graphene, Science 332 (2011) 1537–1541, https://doi.org/10.1126/science.1200770.

[4] M.M. Samy, M.G. Mohamed, S.U. Sharma, S.V. Chaganti, T.H. Mansoure, J.T. Lee, T. Chen, S.W. Kuo, Constructing conjugated microporous polymers containing triphenylamine moieties for high-performance capacitive energy storage, Polymer 264 (2023) 125541, https://doi.org/10.1016/j.polymer.2022.125541.

[5] Y. Shao, M.F. El-Kady, J. Sun, Y. Li, Q. Zhang, M. Zhu, H. Wang, B. Dunn, R. B. Kaner, Design and mechanisms of asymmetric supercapacitors, Chem. Rev. 118 (2018) 9233–9280, https://doi.org/10.1021/acs.chemrev.8b00252.

[6] D. Zhou, Y. Pu, Y. Wang, L. Hu, J. Quan, S. Lan, J. Ma, F. Wang, W. Wan, Y. Tong, R. Lv, H. Xu, H. Peng, M. Yu, L. Chen, Perylene diimide cathode interface layer with siloxane bay-modification for efficient and stable organic solar cells, Chem. Eng. J. 509 (2025) 161155, https://doi.org/10.1016/j.cej.2025.161155.

[7] S. Lan, D. Zhou, Hu Lin, H. Li, Y. Pu, F. Wang, W. Wan, Y. Tong, R. Lv, H. Xu, B. Hu, P. Cheng, Z. Li, L. Chen, Subtly modulating bay sites of perylene diimide cathode interface layer for high-performance and high-stability non-fullerene organic solar cells, Adv. Funct. Mater. 35 (2025) 2419205, https://doi.org/10.1002/adfm.202419205.

[8] D. Zhou, Y. Wang, Y. Li, L. Han, F. Wang, S. Lan, R. Lv, L. Hu, J. Xie, J. Quan, X. Yang, Xu Zhentian, Lie Chen, N-type small molecule electrolyte cathode interface layer with thickness insensitivity for organic solar cells, Nano Energy 128 (2024) 109890, https://doi.org/10.1016/j.nanoen.2024.109890.

[9] W. Chen, D. Zhou, L. Hu, J. Ma, G. Shen, W. Wan, S. Wang, F. Wang, R. Lv, B. Hu, H. Xu, Z. Li, L. Chen, Self-healing and thickness-insensitive perylene diimide-based cathode interfacial layers for organic solar cells, Chem. Eng. J. 521 (2025) 166518, https://doi.org/10.1016/j.cej.2025.166518.

[10] T. Shi, Z. Song, C. Hu, Q. Huang, Y. Lv, L. Miao, L. Gan, D. Zhu, M. Liu, Low-redox-barrier two-electron p-type phenoselenazine cathode for superior zinc-organic batteries, Angew. Chem. Int. Ed. 64 (2025) e202501278, https://doi.org/10.1002/anie.202501278.

[11] P. Liu, Z. Song, Q. Huang, L. Miao, Y. Lv, L. Gan, M. Liu, Multi-H-bonded self-assembled superstructures for ultrahigh-capacity and ultralong-life all-organic ammonium-ion batteries, Energy Environ. Sci. 18 (2025) 5397–5406, https://doi.org/10.1039/D5EE00823A.

[12] Z. Song, Y. Qi Huang, L. Lv, M. Liu Gan, Multi-N-heterocycle donor-acceptor conjugated amphoteric organic superstructures for superior zinc batteries, Angew. Chem. Int. Ed. 64 (2025) e202418237, https://doi.org/10.1002/anie.202418237.

[13] M.M. Samy, M.G. Mohamed, S.W. Kuo, Pyrene-functionalized tetraphenylethylene polybenzoxazine for dispersing single-walled carbon nanotubes and energy storage, Compos. Sci. Technol. 199 (2020) 108360, https://doi.org/10.1016/j.compscitech.2020.108360.

[14] M.G. Mohamed, M.G. Kotp, A.O. Mousa, Y.S. Li, S.W. Kuo, Construction of Fe- and N-doped microporous carbon from ferrocene-based conjugated microporous polymers for supercapacitive energy storage, ACS Appl. Energy Mater. 8 (2025) 2389–2402, https://doi.org/10.1021/acsaem.4c02968.

[15] A. Basit, M.G. Mohamed, S.U. Sharma, S.W. Kuo, Thianthrene- and thianthrene tetraoxide-functionalized conjugated microporous polymers for efficient energy storage, ACS Appl. Polym. Mater. 6 (2024) 12247–12260, https://doi.org/10.1021/acsapm.4c02368.

[16] A. Basit, M.G. Mohamed, M. Ejaz, B.X. Su, H. Manzoor, S.W. Kuo, Boosting supercapacitor energy storage using microporous carbon derived from an octavinylsilsesquioxane and fluorenone-linked porous hybrid polymer, ACS Appl. Energy Mater. 7 (2024) 7505–7516, https://doi.org/10.1021/acsaem.4c01796.

[17] P. Ghasemiahangarani, G. Farhan, D. Del Mundo, T. Schoetz, Charge storage mechanisms in batteries and capacitors: a perspective of the electrochemical interface, Adv. Energy Mater. 15 (2025) 2404704, https://doi.org/10.1002/aenm.202404704.

[18] M.M. Samy, M.G. Mohamed, S.U. Sharma, S.V. Chaganti, J.T. Lee, S.W. Kuo, An ultrastable tetrabenzonaphthalene-linked conjugated microporous polymer functioning as a high-performance electrode for supercapacitors, J. Taiwan Inst. Chem. Eng. 158 (2024) 104750, https://doi.org/10.1016/j.jtice.2023.104750.

[19] A.O. Mousa, S.U. Sharma, S.V. Chaganti, T.H. Mansoure, P.N. Singh, M. Ejaz, C. H. Chuang, J.T. Lee, S.W. Kuo, Mohamed Gamal Mohamed, Designing strategically functionalized conjugated microporous polymers with pyrene and perylenetetracarboxylic dianhydride moieties with single-walled carbon nanotubes to enhance supercapacitive energy storage efficiency, J. Power Sources 608 (2024) 234624, https://doi.org/10.1016/j.jpowsour.2024.234624.

[20] M.G. Mohamed, C.C. Chen, M. Ibrahim, A.O. Mousa, M.H. Elsayed, Y. Ye, S.W. Kuo, Tetraphenylanthraquinone and dihydroxybenzene-tethered conjugated microporous polymer for enhanced CO_2 uptake and supercapacitive energy storage, JACS Au 4 (2024) 3593–3605, https://doi.org/10.1021/jacsau.4c00537.

[21] H.R. Khan, A.L. Ahmad, Supercapacitors: overcoming current limitations and charting the course for next-generation energy storage, J. Ind. Eng. Chem. 141 (2024) 46–66, https://doi.org/10.1016/j.jiec.2024.07.014.

[22] A.G. Olabi, A. Qaisar, A.A. Makky, M.A. Abdelkareem, Supercapacitors as next generation energy storage devices: properties and applications, Energy 248 (2022) 123617, https://doi.org/10.1016/j.energy.2022.123617.

[23] M.G. Mohamed, B.X. Su, S.W. Kuo, Robust nitrogen-doped microporous carbon via crown ether-functionalized benzoxazine-linked porous organic polymers for enhanced CO_2 adsorption and supercapacitor applications, ACS Appl. Mater. Interfaces 16 (2024) 40858–40872, https://doi.org/10.1021/acsami.4c05645.

[24] M.G. Mohamed, M. Ibrahim, N.P. Chen, A. Basit, Y.C. Kao, A.O. Mousa, M. M. Samy, S.W. Kuo, Tetrabenzonaphthalene and redox-active anthraquinone-linked conjugated microporous polymers as organic electrodes for enhanced energy storage efficiency, ACS Appl. Energy Mater. 7 (2024) 5582–5593, https://doi.org/10.1021/acsaem.4c01276.

[25] S.V. Chaganti, S.U. Sharma, M. Ibrahim, A. Basit, P.N. Singh, S.W. Kuo, M. G. Mohamed, Redox-active a pyrene-4, 5,9,10-tetraone and thienyltriazine-based conjugated microporous polymers for boosting faradaic supercapacitor energy storage, J. Power Sources 627 (2025) 235848, https://doi.org/10.1016/j.jpowsour.2024.235848.

[26] N.R. Chodankar, H.D. Pham, A.K. Nanjundan, J.F.S. Fernando, K. Jayaramulu, D. Golberg, Y. Han, D.P. Dubal, True meaning of pseudocapacitors and their performance metrics: asymmetric versus hybrid supercapacitors, Small 16 (2020) 2002806, https://doi.org/10.1002/smll.202002806.

[27] X. Guan, Y. Zhao, H. Pei, M. Zhao, Y. Wang, X. Zhou, M.G. Mohamed, S.W. Kuo, Y. Ye, Metalloporphyrin conjugated porous polymer in-situ grown on a Celgard separator as multifunctional polysulfide barrier and catalyst for high-performance Li-S batteries, Chem. Eng. J. 473 (2023) 144733, https://doi.org/10.1016/j.cej.2023.144733.

[28] H.W. Park, K.C. Roh, Recent advances in and perspectives on pseudocapacitive materials for supercapacitors–a review, J. Power Sources 557 (2023) 232558, https://doi.org/10.1016/j.jpowsour.2022.232558.

[29] C.V.V.M. Gopi, S. Alzahmi, M.Y. Al-Haik, Y.A. Kumar, F. Hamed, Y. Haik, I. M. Obaidat, Recent advances in pseudocapacitive electrode materials for high energy density aqueous supercapacitors: combining transition metal oxides with carbon nanomaterials, Mater. Today Sustain. 28 (2024) 100981, https://doi.org/10.1016/j.mtsust.2024.100981.

[30] B. Arumugam, G. Mayakrishnan, S.K.S. Manickavasagam, S.C. Kim, R. Vanaraj Kim, An overview of active electrode materials for the efficient high-performance supercapacitor application, Crystals 13 (2023) 1118, https://doi.org/10.3390/cryst13071118.

[31] M.Y. Ho, P.S. Khiew, D. Isa, T.K. Tan, W.S. Chiu, C.H. Chia, A review of metal oxide composite electrode materials for electrochemical capacitors, Nano 9 (2014) 1430002, https://doi.org/10.1142/S1793292014300023.

[32] A. Basit, Y.C. Kao, Y.A. El-Ossaily, S.W. Kuo, M.G. Mohamed, Rational engineering and synthesis of pyrene and thiazolo[5,4-d] thiazole-functionalized conjugated microporous polymers for efficient supercapacitor energy storage, J. Mater. Chem. A 12 (2024) 30508–30521, https://doi.org/10.1039/D4TA05908E.

[33] M.G. Mohamed, A.F.M. EL-Mahdy, M.G. Kotp, S.W. Kuo, Advances in porous organic polymers: syntheses, structures, and diverse applications, Mater. Adv. 3 (2022) 707–733, https://doi.org/10.1039/D1MA00771H.

[34] M.M. Samy, I.M.A. Mekhemer, M.G. Mohamed, M.H. Elsayed, K.H. Lin, Y.K. Chen, T.L. Wu, H.H. Chou, S.W. Kuo, Conjugated microporous polymers incorporating thiazolo [5,4-d] thiazole moieties for sunlight-driven hydrogen production from water, Chem. Eng. J. 446 (2022) 137158, https://doi.org/10.1016/j.cej.2022.137158.

[35] S.Y. Chang, A.M. Elewa, M.G. Mohamed, I.M.A. Mekhemer, M.M. Samy, K. Zhang, H.H. Chou, S.W. Kuo, Rational design and synthesis of bifunctional dibenzo [g,p] chrysene-based conjugated microporous polymers for energy storage and visible light-driven photocatalytic hydrogen evolution, Mater. Today Chem. 33 (2023) 101680, https://doi.org/10.1016/j.mtchem.2023.101680.

[36] M.G. Mohamed, S.U. Sharma, P.T. Wang, M. Ibrahim, M.H. Lin, C.L. Liu, M. Ejaz, H.J. Yen, S.W. Kuo, Construction of fully π-conjugated, diyne-linked conjugated microporous polymers based on tetraphenylethene and dibenzo [g, p] chrysene units for energy storage, Polym. Chem. 15 (2024) 2827–2839, https://doi.org/10.1039/D4PY00421C.

[37] J. Lee, A.I. Cooper, Advances in conjugated microporous polymers, Chem. Rev. 120 (2020) 2171–2214, https://doi.org/10.1021/acs.chemrev.9b00399.

[38] W.T. Chung, I.M.A. Mekhemer, M.G. Mohamed, A.M. Elewa, A.F.M. EL-Mahdy, H. H. Chou, S.W. Kuo, K.C.W. Wu, Recent advances in metal/covalent organic frameworks-based materials: their synthesis, structure design and potential applications for hydrogen production, Coord. Chem. Rev. 483 (2023) 215066, https://doi.org/10.1016/j.ccr.2023.215066.

[39] Y.C. Kao, K.T. Yeh, M.G. Mohamed, H. Karim, W.H. Su, S.W. Kuo, Structural modulation via mesoporous silica templating in covalent organic frameworks: converting functional aspects for adsorption behavior, Sep. Purif. Technol. 375 (2025) 133827, https://doi.org/10.1016/j.seppur.2025.133827.

[40] I.M.A. Mekhemer, A.M. Elewa, M.M. Elsenety, M.M. Samy, M.G. Mohamed, A. F. Musa, T.F. Huang, T.C. Wei, S.W. Kuo, B.H. Chen, S.D. Yang, H.H. Chou, Self-condensation for enhancing the hydrophilicity of covalent organic polymers and photocatalytic hydrogen generation with unprecedented apparent quantum yield up to 500 nm, Chem. Eng. J. 497 (2024) 154280, https://doi.org/10.1016/j.cej.2024.154280.

[41] M.G. Mohamed, A.M. Elewa, N.P. Chen, A.A.K. Mohammed, S.W. Kuo, Construction of malononitrile-functionalized conjugated microporous polymers as adsorbents for effective adsorption of Rhodamine B and density functional theory perspective, Colloids Surf. A Physicochem. Eng. Asp. 721 (2025) 137214, https://doi.org/10.1016/j.colsurfa.2025.137214.

[42] M.G. Mohamed, E.C. Atayde Jr., B.M. Matsagar, J. Na, Y. Yamauchi, K.C.W. Wu, S. W. Kuo, Construction hierarchically mesoporous/microporous materials based on block copolymer and covalent organic framework, J. Taiwan Inst. Chem. Eng. 112 (2020) 180–192, https://doi.org/10.1016/j.jtice.2020.06.013.
[43] S.A. Ali, I. Sadiq, T. Ahmad, Superlative porous organic polymers for photochemical and electrochemical CO_2 reduction applications: from synthesis to functionality, Langmuir 40 (2024) 10414–10432, https://doi.org/10.1021/acs.langmuir.4c00310.
[44] Q. Zhao, Q. Zhang, Y. Xu, A. Han, H. He, H. Zheng, W. Zheng, H. Lei, U.P. Apfel, R. Cao, Improving active site local proton transfer in porous organic polymers for boosted oxygen electrocatalysis, Angew. Chem. Int. Ed. 63 (2024) e202414104, https://doi.org/10.1002/anie.202414104.
[45] P. Kaur, J.T. Hupp, S.T. Nguyen, Porous organic polymers in catalysis: opportunities and challenges, ACS Catal. 1 (2011) 819–835, https://doi.org/10.1021/cs200131g.
[46] Y.B. Zhou, Z.P. Zhan, Conjugated microporous polymers for heterogeneous catalysis, Chem. Asian J. 13 (2018) 9–19, https://doi.org/10.1002/asia.201701107.
[47] M.G. Kotp, M.G. Mohamed, P.T. Wang, A.E. Hassan, A.M. Elewa, S.W. Kuo, Unlocking the potential of N,N,N',N'-Tetraphenyl benzidine based on conjugated microporous polymers for Rhodamine B adsorption: A synergistic experimental and density functional theory perspective, ACS Polymers Au 5 (2025) 379–393, https://doi.org/10.1021/acspolymersau.5c00025.
[48] P. Xie, C. Han, S. Xiang, S. Jin, M. Ge, C. Zhang, J.X. Jiang, Toward high-performance dibenzo[g,p]chrysene-based conjugated polymer photocatalysts for photocatalytic hydrogen production through donor-acceptor-acceptor structure design, Chem. Eng. J. 459 (2023) 141553, https://doi.org/10.1016/j.cej.2023.141553.
[49] H. Ou, X. Chen, L. Lin, Y. Fang, X. Wang, Biomimetic donor–acceptor motifs in conjugated polymers for promoting exciton splitting and charge separation, Angew. Chem. Int. Ed. 57 (2018) 8729–8733, https://doi.org/10.1002/anie.201803863.
[50] C. Shu, C. Han, X. Yang, C. Zhang, Y. Chen, S. Ren, F. Wang, F. Huang, J.X. Jiang, Boosting the photocatalytic hydrogen evolution activity for D–π–A conjugated microporous polymers by statistical copolymerization, Adv. Mater. 33 (2021) 2008498, https://doi.org/10.1002/adma.202008498.
[51] M.G. Mohamed, M.H. Elsayed, C.J. Li, A.E. Hassan, I.M.A. Mekhemer, A.F. Musa, M.K. Hussien, L.C. Chen, K.H. Chen, H.H. Chou, S.W. Kuo, Reticular design and alkyne bridge engineering in donor–π–acceptor type conjugated microporous polymers for boosting photocatalytic hydrogen evolution, J. Mater. Chem. A 12 (2024) 7693–7710, https://doi.org/10.1039/D3TA07309B.
[52] J. Xiao, Z. Xiao, J. Hu, X. Gao, M. Asim, L. Pan, C. Shi, X. Zhang, J.J. Zou, Rational design of alkynyl-based linear donor− π–acceptor conjugated polymers with accelerated exciton dissociation for photocatalysis, Macromolecules 55 (2022) 5412–5421, https://doi.org/10.1021/acs.macromol.2c00885.
[53] M.G. Mohamed, I.M.A. Mekhemer, A.F.H. Selim, A. Katsamitros, D. Tasis, A. Basit, H.H. Chou, S.W. Kuo, Molecular engineering of donor–acceptor-type conjugated microporous polymers for dual effective photocatalytic production of hydrogen and hydrogen peroxide, Mater. Horiz. 12 (2025) 5917–5928, https://doi.org/10.1039/D5MH00735F.
[54] M.G. Mohamed, B. Halder, P.N. Singh, A.A.K. Mohammed, P. Elumalai, S.W. Kuo, Molecular engineering and synergistic redox-active hexaazatrinaphthalene and pyrene-based conjugated microporous polymers for superior faradaic supercapacitor energy storage, Chem. Eng. J. 520 (2025) 165892, https://doi.org/10.1016/j.cej.2025.165892.
[55] G. Wang, N. Tahir, I. Onyshchenko, N.D. Geyter, R. Morent, K. Leus, P.V.D. Voort, Novel hexaazatrinaphthalene-based covalent triazine frameworks as high-performance platforms for efficient carbon capture and storage, Microporous Mesoporous Mater. 290 (2019) 109650, https://doi.org/10.1016/j.micromeso.2019.109650.
[56] J. Wang, C.S. Chen, Y. Zhang, Hexaazatrinaphthylene-based porous organic polymers as organic cathode materials for lithium-ion batteries, ACS Sustain. Chem. Eng. 6 (2018) 1772–1779, https://doi.org/10.1021/acssuschemeng.7b03165.
[57] Y. Kou, Y. Xu, Z. Guo, D. Jiang, Supercapacitive energy storage and electric power supply using an aza-fused π-conjugated microporous framework, Angew. Chem. Int. Ed. 50 (2011) 8753–8757, https://doi.org/10.1002/anie.201103493.
[58] P. Xu, X. Jin, B. Zhang, X. Wang, D. Liu, An insoluble amino-functionalized hexaazatriphenylene as stable organic cathode in lithium-ion batteries, Batteries 9 (2023) 85, https://doi.org/10.3390/batteries9020085.
[59] A. VahidMohammadi, J. Rosen, Y. Gogotsi, The world of two-dimensional carbides and nitrides (MXenes), Science 372 (2021) eabf1581, https://doi.org/10.1126/science.abf1581.
[60] Z. Ling, C.E. Ren, M.-Q. Zhao, J. Yang, J.M. Giammarco, J. Qiu, M.W. Barsoum, Y. Gogotsi, Flexible and conductive MXene films and nanocomposites with high capacitance, Proc. Natl. Acad. Sci. USA 111 (2014) 16676–16681, https://doi.org/10.1073/pnas.1414215111.
[61] E. Sivasurya, M. Elancheziyan, F. Ashamary, G. Maheswari, A. Raji, M. G. Mohamed, A. Padmanaban, K. Won, P.K. Kalambate, S.W. Kuo, D. Manoj, Achieving high energy density with all pseudocapacitive asymmetric materials as energy storage device: metallic ruthenium confined in MOF-derived N-doped porous carbon as positive and free-standing Ti_3C_2 film as negative electrode, J. Power Sources 662 (2026) 238813, https://doi.org/10.1016/j.jpowsour.2025.238813.
[62] D. Spurling, H. Krüger, N. Kohlmann, F. Rasch, M.P. Kremer, L. Kienle, R. Adelung, V. Nicolosi, F. Schütt, 3D networked MXene thin films for high performance supercapacitors, Energy Storage Mater. 65 (2024) 103148, https://doi.org/10.1016/j.ensm.2023.103148.
[63] M. Gao, F. Wang, S. Yang, A. Gaetano Ricciardulli, F. Yu, J. Li, J. Sun, R. Wang, Y. Huang, P. Zhang, X. Lu, Engineered 2D MXene-based materials for advanced supercapacitors and micro-supercapacitors, Mater. Today 72 (2024) 318–358, https://doi.org/10.1016/j.mattod.2023.12.009.
[64] M.G. Mohamed, T.C. Chen, S.W. Kuo, Solid-state chemical transformations to enhance gas capture in benzoxazine-linked conjugated microporous polymers, Macromolecules 54 (2021) 5866–5877, https://doi.org/10.1021/acs.macromol.1c00736.
[65] M.G. Mohamed, W.C. Chang, S.W. Kuo, Crown ether- and benzoxazine-linked porous organic polymers displaying enhanced metal ion and CO_2 capture through solid-state chemical transformation, Macromolecules 55 (2022) 7879–7892, https://doi.org/10.1021/acs.macromol.2c01216.
[66] M.G. Mohamed, S.U. Sharma, C.H. Yang, M.M. Samy, A.A.K. Mohammed, S. V. Chaganti, J.T. Lee, S.W. Kuo, Anthraquinone-enriched conjugated microporous polymers as organic cathode materials for high-performance lithium-ion batteries, ACS Appl. Energy Mater. 4 (2021) 14628–14639, https://doi.org/10.1021/acsaem.1c03270.
[67] T.H. Weng, M.G. Mohamed, S.U. Sharma, I.M.A. Mekhemer, H.H. Chou, S.W. Kuo, Rationally engineered ultrastable three-dimensional (3D) conjugated microporous polymers containing triptycene, tetraphenylethene, and benzothiadiazole units as exceptional high-performance organic electrodes for supercapacitors, ACS Appl. Energy Mater. 6 (2023) 9012–9024, https://doi.org/10.1021/acsaem.3c01933.
[68] S. Xu, G. Wang, B.P. Biswal, M. Addicoat, S. Paasch, W. Sheng, X. Zhuang, E. Brunner, T. Heine, R. Berger, X. Feng, A nitrogen-rich 2D sp^2-carbon-linked conjugated polymer framework as a high-performance cathode for lithium-ion batteries, Angew. Chem. Int. Ed. 58 (2019) 849–853, https://doi.org/10.1002/anie.201812685.
[69] L. Xu, L. Zhenhu, Y. Zhang, H. Guo, M. Zou, H. Li, Y. Liu, S. Liu, Stable hexaazatrinaphthylene-based covalent organic framework as high-capacity electrodes for aqueous hybrid supercapacitors, Energy Mater. 5 (2025) 500036, https://doi.org/10.20517/energymater.2024.127.
[70] P. Xu, S. Ouyang, Q. Bai, Q. Ma, Y. Zhu, A hexaazatriphenylene-based porous organic polymer for high performance supercapacitor, J. Polym. Chem. 62 (2024) 1647–1653, https://doi.org/10.1002/pol.20230256.
[71] L. Jeftic, R.N. Adams, Electrochemical oxidation pathways of benzo[a]pyrene, J. Am. Chem. Soc. 92 (1970) 1332–1337, https://doi.org/10.1021/ja00708a037.